https://doi.org/10.1016/j.jpowsour.2018.08.038

Manuscript for publication (Journal of Power Sources)

Mathematical Modeling of a Proton-Conducting Solid Oxide Fuel Cell with Current Leakage

Ji-Hao Zhang[†ab], Li-Bin Lei[†b], Di Liu[c], **Fu-Yun Zhao**[a,*], Meng Ni[d], Fanglin Chen[b]

a) School of Power and Mechanical Engineering, **Wuhan University**, Wuhan, Hubei Province, P. R. China

b) Department of Mechanical Engineering, **University of South Carolina**, Columbia, USA

c) College of Pipeline and Civil Engineering, **China University of Petroleum**, Qingdao, Shandong Province, P. R. China

d) Department of Building and Real Estate, **The Hong Kong Polytechnic University**, Hung Hom, Kowloon, Hong Kong, P. R. China

[*] Corresponding author. Tel: +86 1 860 274 8575; fax: +86 27 68756661
School of Power and Mechanical Engineering, Wuhan University, Luo-Jia-Shan, 430072, Wuhan, Hubei Province, P. R. China
E-mail address: fyzhao@whu.edu.cn (F.Y. Zhao), chenfa@cec.sc.edu(Frank Chen)
[†] These authors contributed equally to this work.

Abstract and keywords

Abstract

In this work, a framework of charge transports in proton-conducting solid oxide fuel cells (H-SOFCs) with considering current leakage is developed by assuming four electrode reactions. Current leakage occurs when electron holes pass through the electrolyte and combine with electrons at the anode side. An analytical solution of leakage currents is proposed depending on the Nernst-Planck equation. On the basis of the analysis expression, a mathematical model of H-SOFCs is proposed, which can provide the information about current-voltage characteristics, leakage current density, Faraday and energy efficiencies. Furthermore, H-SOFCs with the $BaZr_{0.8}Y_{0.2}O_3$ electrolyte are fabricated and tested, and the proposed model well reproduces the experimental data. The simulation results indicate that current leakage primarily affects the H-SOFC performance when the output voltage is close to the OCV. Both Faraday efficiencies and energy efficiencies decrease with increasing operating temperatures due to the existence of current leakage.

Keywords

Current Leakage; SOFC; Proton-conducting; modeling; Nernst-Planck equation; Faraday and energy efficiencies

Nomenclature

Nomenclature			
		Greek symbols	
D	Diffusion coefficient of species, m^2/s	σ	Conductivity, S/m
		τ	Thickness, μm
E	Activation energy , J/mol	ϕ	Electrostatic potential, V
F	Faraday constant, 96485 C/mol	ε	Electrode porosity
J	Current density, A/m^2	β	The symmetry factor
J_m	Molar flux, mol/m^2	γ	The pre-exponential factors, A/m^2
k_B	Boltzmann constant, 1.381×10^{-23} J/K	μ	chemical potential, J/mol
		η	Overpotential, V
M	Molecular weight of species, kg/mol	**Subscripts**	
		a (c)	At the anode (cathode) side
n_e	Number of electrons	*ele*	The electrolyte
P	Operating pressure, bar	*i, j*	Species *i, j*
q	Elementary charge, 1.602×10^{-19} C	*k*	Knudsen diffusion
		m	Gas mixture
R	Gas constant, 8.3145 J/(mol K)	*ext*	The external current
T	Temperature, K	*con*	Concentration overpotential
v	Dynamic viscosity, m^2/s	*act*	Activation overpotential
V	Output voltage, V	*ohm*	Ohmic overpotential
y	Volume fractions, m^3/m^3	**Superscripts**	
z	Charge valences	*I*	The electrode-electrolyte interface
		0	The initial condition

Main text

1. Introduction

Fuel cells, which directly convert chemical energy into electrical energy, have been well recognized in recent years as high-efficiency, quiet and environmentally benign energy conversion devices for power generation. Among the various types of fuel cells, solid oxide fuel cells (SOFCs) are considered a promising energy converting technology, which possess several additional advantages such as multi-fuel flexibility, no liquid electrolyte with its attendant material corrosion and the absence of a requirement for precious-metal catalysts [1-3].

In general, there are two types of electrolytes (i.e., oxygen ion and proton conducting electrolytes) for applying to SOFCs at high operating temperatures (HT, 700-1000 °C) and intermediate temperatures (IT, 400-700 °C), respectively [4, 5]. The current oxygen ion conducting SOFC technology, based on yttria-stabilized zirconia (YSZ) electrolytes, requires the cell to operate in the HT range, which results in high energy input, materials compatibility challenges and strict operational complexity. Fortunately, protons migrate easily by the Grotthustype mechanism in the perovskitetype oxide lattice, leading to smaller values of activation energy compared to those of oxygen-ion conductors. Thus, proton conducting solid oxide fuel cells (H-SOFCs) should possess larger conductivity values in the IT range. In addition, H-SOFCs also constitute a promising alternative for the following reasons: the fuel would not be diluted during the operating process and higher Nernst potential and fuel utilization can be expected; the concentration

overpotential can be remarkably reduced within anode-supported H-SOFCs, due to a greater diffusion coefficient of hydrogen [6-8].

Current leakage occurs when perovskite-type materials are used as electrolytes in H-SOFCs. The general formula of perovskite-type oxides can be written as $AB_{1-x}M_xO_{3-d}$. Substituting in the B site, the M dopant cation creates oxygen vacancies [6, 7]. In other words, the hydroxide defects can automatically dissociate and generate free water and oxygen vacancy [6],

$$2OH_O^{\bullet} \rightarrow H_2O + O_O^{\times} + V_O^{\bullet\bullet} \quad (1)$$

Then the oxygen vacancy can greatly contribute to the conduction of electron holes in the oxidizing environment [9, 10].

$$V_O^{\bullet\bullet} + 0.5O_2 \rightarrow 2h^{\bullet} + O_O^{\times} \quad (2)$$

Taking Y-doped $BaZrO_3$ (BZY) as an example, conduction of electron holes is enhanced significantly in a pure oxygen atmosphere [11]. In most cases, the cathode side is exposed to the stationary air with high oxygen potential during operation, and thereby the electron hole conductions are considerable in varieties of operating conditions. Furthermore, transport numbers, which include the ratio of electron hole conductivities and total conductivities, have been widely investigated by impedance spectrum technology in recent researches [10, 12 and 13]. These studies reported that the electronic transport can be in identical order of magnitude as ionic transports. Hence, current leakage can lead to remarkable decreases of open circuit voltages and cell efficiencies.

There have been extensive modeling studies on the H-SOFCs in recent years, which can describe all overpotential losses as well as current-voltage curves from macroscopic view. Researchers [14-17] developed the basic mathematical models for H-SOFCs using hydrogen as fuel gases. With these models, the influences of cell configurations, operating temperature and gas pressure upon the performance of H-SOFCs can be effectively predicted. More recently, methane [18-21] or ammonia [22-23] fed H-SOFCs with direct internal reforming had attracted considerable interest due to their excellent hydrogen carrier performance. Nevertheless, all the above modeling works did not consider current leakage in their electrochemical model. Hence, a full fuel cell model with current leakage is necessary for the progress of H-SOFCs.

Additionally, some studies attempted to analyze the multiple charged defects chemistry from mesoscopic view [24-28]. The defects in the Triple Phases Boundary (TPB), including protons, oxide vacancies, electron holes together with electrons, were assumed to interact with gas environments. Based on the local defect-chemical equilibrium model [24-26], defect concentrations can be estimated with the known kinetics parameters. Then, the fluxes of electron holes or electrons through solid electrolytes can be calculated by the Nernst-Planck equation, charge conservation and Gauss's Law [27-28]. However, these researches mainly forced on the multiple charged defects transport phenomena inside the ceramic electrolyte. And they did not propose a mathematical model to predict the performance of the full H-SOFCs, such as the current-voltage (J-V) characteristic and types of overpotentials. Therefore, there is a

great gap between the macroscopic and mesoscopic investigations for H-SOFCs.

In this work, a framework of charge transports in H-SOFCs with the Y-doped BaZrO3 electrolyte is developed by assuming four electrode reactions. Based on such framework, the defect electrochemical potentials are expressed by the corresponding gas chemical potentials. Simultaneously, the Nernst-Planck equation is implemented to describe proton and electron hole transports through the electrolyte. Finally, a mathematical model is proposed by accounting for coupled interactions between porous media transport in the electrodes, electrochemical polarization in TPB, proton conduction and current leakage in the electrolyte. This study can fill the gap between the macroscopic and mesoscopic investigations on H-SOFCs and provide some theoretical guidelines for the design and optimization of the H-SOFCs with current leakage.

2. Experimental Investigation

The $BaZr_{0.8}Y_{0.2}O_3$ powders were synthesized by a combined EDTA-citric acid method with Metal nitrate precursors $Ba(NO_3)_2$, $ZrO(NO_3)_2{\cdot}xH_2O$ and $Y(NO_3)_2{\cdot}6H_2O$. NiO powders, BZY powders and carbon black were used to prepare the NiO-BZY electrode substrates (10.3 mm in diameter and 0.3 mm in thickness, after sintering at 1450 ^oC) by dry-pressing and then firing at 600 ^oC for 2 h. The BZY electrolyte layer was deposited on the NiO-BZY substrates using the drop-coating method, and then was sintered at 1450 ^oC for 5 h. The $(La_{0.60}Sr_{0.40})_{0.95}Co_{0.20}Fe_{0.80}O_{3-x}$ (LSCF) cathode with an

effective area of 0.33 cm^2 was applied onto the surface of the BZY electrolyte layer by using the LSCF ink and brush painting method and then sintering at 1000 ^oC for 2 h. Furthermore, the $Pr_2Ni_{0.5}Mn_{0.5}O_{4+\delta}$ solution, which was prepared by dissolving $Pr(NO_3)_3 \cdot 6H_2O$, $Ni(NO_3)_2$ and $Mn(NO_3)_2 \cdot 6H_2O$, was impregnated on the surface of the LSCF cathode to form $PrNi_{0.5}Mn_{0.5}O_3$ (PNM) nanoparticles [29].

The schematic diagram of the cell test setup is similar to our previous work [30]: the prepared single cells were attached to one end of an alumina tube using an electrical conductive paste. Ag wires were used as the cathode and anode lead wire and were attached to the electrodes with Ag paste. High temperature ceramic adhesives were then applied outside the attached cells to avoid gas leaking. After NiO was reduced to Ni in situ by flowing H_2, the cell performance was measured at 550–700 ^oC by changing an external load. J–V characteristics of the anode-supported cell were evaluated using humidified hydrogen (3 vol% H_2O) as fuel (with a fuel flow rate of 30 ml/min) and ambient air as the oxidant. The fracture surfaces of the cell after the electrochemical test were examined by scanning with an electron microscope, with a representative image shown as Fig. 1. The thickness of each layer was determined from the SEM micrographs.

3. Mathematical Modeling

Due to axisymmetric button fuel cells were fabricated and tested in this work, the current densities can be assumed uniform both in the axial and the radial directions. A

one-dimensional framework of charge transports in an H-SOFC is developed, as shown in Fig.2. In this model, protons and electron holes are the only mobile charges, and electrochemical reactions are assumed to occur only in the TPB.

3.1. Electrochemical reactions in TPB

ANODE

Through quantities of reviewing, four electrode reactions (*RI-RIV*) were adopted in our model. At the anode of the H-SOFC, the hydrogen oxidation produces protons and electrons near the nickel and BZY particles, as illustrated as Reaction I (*RI*) in Fig. 2,

$$H_2 \xrightarrow{Ni} 2H^+ + 2e^- \tag{3}$$

Although the actual reaction pathway could be composite and uncertain [31], the proton and electron can be regarded as the final products. Then, the protons migrate through the BZY particles to the electrolyte, and combine with lattice oxygen. The formations of hydroxide defects occur via the following reaction [32],

$$2H^+ + 2O_O^\times \rightarrow 2OH_O^\bullet \tag{4}$$

In fact, quite few of oxygen ions move across the dense BZY electrolyte in the IT range and only protons jump from one lattice oxygen to another by Rotational Motion [6, 7].

For the actual working state, in which current leakage takes place within the H-SOFC, most electrons are collected by the interconnect to supply power for the external applications and the other electrons react with electron holes, as indicated as Reaction II (*RII*) in Fig. 2,

$$h^\bullet + e^- \rightarrow 0 \tag{5}$$

To quantitatively describe the proportion of electrons supplying power to external applications, Faraday efficiency is introduced as,

$$t = \frac{J_{ext}}{J_{ext} + J_{h^{\bullet}}} \tag{6}$$

where J_{ext} and $J_{h^{\cdot}}$ are the external current and the electron hole current, respectively.

CATHODE

In the area where there is enough electrons, the oxygen molecules from the surrounding atmosphere are absorbed on the mixed O^{2-}/e^{-} conducting phase (LSCF) surface, dissociate, and react with electrons to form O^{2-} ions [32],

$$0.5O_2 + 2e^{-} \rightarrow O^{2-} \tag{7}$$

Then, the water formation reaction between hydroxide defects and oxygen ions has to be considered,

$$2OH_O^{\bullet} + O^{2-} \rightarrow H_2O + 2O_O^{\times} \tag{8}$$

As demonstrated as Reaction III (*RIII*) in Fig. 2, in the situation there is enough electrons, the simplified overall half reaction between proton and oxygen can be expressed as follows,

$$2H^{+} + 0.5O_2 + 2e^{-} \rightarrow H_2O \tag{9}$$

There are not always enough electrons through the cathode-electrolyte interfaces, due to the existence of current leakage. As mentioned in the introduction, oxygen incorporation occurs in the oxidizing environment, which produces a quantity of holes as shown as Eq. (2). Consequently, the simplified overall half reactions between proton and oxygen by lack of enough electrons could be expressed as Eq. (10), as illustrated as

Reaction IV (*RIV*) in Fig. 2,

$$2H^+ + 0.5O_2 \rightarrow H_2O + 2h^\bullet \quad (10)$$

Overall, there are two charge transport circles in the H-SOFC as demonstrated in Fig. 2, including the external circle and the inner circle: the external circle is formed when t×100% electrons flow from the anode to the cathode through the external circuit (J_{ext}), and react with t×100% protons and oxygen molecules to form steam, as illustrated as *RIII*; the inner circle is created when the surplus (1-t) ×100 % protons react with oxygen molecules, producing water and electron holes, as shown as *RIV*. The electron holes then pass through the dense BZY electrolyte and react with the surplus (1-t) ×100 % electrons, as shown as *RII*.

3.2. Charge transports in the electrolyte

According to the Nernst-Planck equation, the molar fluxes of protons and electron holes through the electrolyte can be described as [33, 34]:

$$J_{m,i} = -D_i \nabla c_i - \frac{\sigma_i}{z_i q} \nabla \phi \quad i = H^+, h^\bullet \quad (11)$$

Where D is the diffusivity, c is the density of mobile ions, σ is the conductivity, z is the valence of charges, q is the elementary charge and ϕ is the electrostatic potential. The Nernst-Einstein relation is [33]:

$$D_i = \frac{k_B T}{(z_i q)^2 c_i} \sigma_i \quad (12)$$

where k_B is the Boltzmann constant. Chemical potential is related to the density of mobile ions [33, 35],

$$\mu_i = \mu_i^0 + RT \ln c_i \tag{13}$$

where R is the gas constant. Substituting Eqs. (12) and (13) into Eq. (11), the current densities of protons and electron holes occurring in the electrolyte can be expressed respectively as [33, 36]:

$$J_{H^+} = -\frac{\sigma_{H^+}}{F} \nabla \mu_{H^+} - \sigma_{H^+} \nabla \phi \tag{14}$$

$$J_{h^\bullet} = -\frac{\sigma_{h^\bullet}}{F} \nabla \mu_{h^\bullet} - \sigma_{h^\bullet} \nabla \phi \tag{15}$$

Through eliminating ϕ, the following relation can be achieved:

$$\frac{J_{h^\bullet}}{\sigma_{h^\bullet}} - \frac{J_{H^+}}{\sigma_{H^+}} = \frac{1}{F} (\nabla \mu_{H^+} - \nabla \mu_{h^\bullet}) \tag{16}$$

Here the quasi-equilibrium state is assumed for reactions *I-IV*; thus protons and electron holes are respectively in equilibrium between electrolyte and the electrodes, i.e.,

$$2\mu_{H^+}^a - 2\mu_{h^\bullet}^a = \mu_{H_2}^a \tag{17}$$

$$2\mu_{H^+}^c - 2\mu_{h^\bullet}^c = \mu_{H_2O}^c - 0.5\mu_{O_2}^c = \mu_{H_2}^c \tag{18}$$

Integrating Eq. (16) throughout the electrolyte and combining Eq. (17) and Eq. (18) to eliminate electrochemical potentials, the following expression can be obtained,

$$J_{h^\bullet} \frac{\tau_{ele}}{\sigma_{h^\bullet}} - J_{H^+} \frac{\tau_{ele}}{\sigma_{H^+}} = \frac{RT}{2F} \ln \frac{P_{H_2}^a}{P_{H_2}^c} \tag{19}$$

where τ_{ele} represents the thickness of the electrolyte and the assumption of uniform conductivities throughout the electrolyte is adopted for a certain temperature. This equation describing the transport of protons and electron holes in the electrolyte is essentially similar to those reported about oxygen iron conducting SOFCs [33, 34 and

35].

The external current direction from cathode to anode is defined as positive. Thus, the proton current is negative and the electron hole current is positive based on Kirchhoff's law, as illustrated in Fig. 2. For a given external current density, J_{ext}, the following relation is achieved,

$$J_{H^+} = -\left(J_{h^\bullet} + J_{ext}\right) \tag{20}$$

Combining Eq. (19) with Eq. (20), the analytical solution of leakage currents for an H-SOFC is expressed as,

$$J_{h^\bullet} = \left[\frac{RT}{2F} \ln \frac{P_{H_2}^a}{P_{H_2}^c} - J_{ext} \frac{\tau_{ele}}{\sigma_{H^+}} \right] / \left(\frac{\tau_{ele}}{\sigma_{h^\bullet}} + \frac{\tau_{ele}}{\sigma_{H^+}} \right) \tag{21}$$

On the basis of this analytical solution, current leakage can be calculated for a given external current. Furthermore, the proton currents as well as the polarization losses can be more precisely predicted with considering current leakage.

3.3 The electrochemical model for H-SOFCs

The potential balance equation, considering all overpotential losses that occur during operation, can be written as follows [14, 15 and 18],

$$V_{out} = E_{eq} - \eta_{ohmic} - \eta_{act,a} - \eta_{act,c} - \eta_{conc,a} - \eta_{conc,c} \tag{22}$$

where η_{ohm} is the ohmic overpotential; $\eta_{act,a}$, $\eta_{act,c}$, $\eta_{conc,a}$ and $\eta_{conc,c}$ are respectively the activation overpotentials and concentration overpotentials at the anode and cathode.

The equilibrium voltage of H-SOFCs fed pure hydrogen as fuel can be expressed by the Nernst equation [15, 19],

$$E_{eq} = 1.253 - 2.4516 \times 10^{-4} T + \frac{RT}{2F} \ln\left[\frac{P_{H_2}^0 (P_{O_2}^0)^{1/2}}{P_{H_2O(C)}^0} \right] \quad (23)$$

where P^0 is the equilibrium pressure of the electrode surface.

According to Ohm's law, the Ohmic overpotential of H-SOFCs is proportional to the proton current density (J_{H+}) as shown below [14, 15 and 19],

$$\eta_{ohm} = J_{H^+} \frac{\tau_{ele}}{\sigma_{H^+}} \quad (24)$$

An important point to note is that the proton conductivity as well as the electronic holes conductivity of the BZY electrolyte varies as a strong function of temperature based on the defect equilibrium model [37],

$$\sigma_{H^+} = \sigma_{0,H^+} T^{-1} \exp\left(-\frac{E_{H^+}}{k_B T} \right), \quad \sigma_{h^\cdot} = \sigma_{0,h^\cdot} T^{-1} \exp\left(-\frac{E_{h^\cdot}}{k_B T} \right) \quad (25)$$

where E_{H+} and $E_{h^\cdot}$ are the activation energies for the carrier of protons and electronic holes respectively [11, 37]; $\sigma_{0,H+}$ and $\sigma_{0,h^\cdot}$ are the pre-factors obtained by fitting the experimental data.

The activation overpotentials are related to the proton current density, and usually are expressed by the non-linear Butler–Volmer equation in implicit form [14-18],

$$J_{H^+} = J_{0,i} \left[\exp\left(\beta_i \frac{Fn_{e,i}}{RT} \eta_{act,i} \right) - \exp\left(-(1-\beta_i) \frac{Fn_{e,i}}{RT} \eta_{act,i} \right) \right], \quad i = a, c. \quad (26)$$

In electrochemistry, $J_{0,i}$ represents the readiness of an electrode to proceed with an electrochemical reaction. The exchange current density can be expressed as [20, 38],

$$J_{0,a} = \gamma_a \exp(-E_{act,a} / RT), \quad J_{0,c} = \gamma_c \exp(-E_{act,c} / RT) \quad (27)$$

where γ_a and γ_c represent the pre-exponential factors of anode and cathode, respectively;

$E_{act,a}$ and $E_{act,c}$ are the activation energy levels at the anode and cathode, respectively.

For H-SOFCs, the concentration overpotentials can be expressed in terms of the gas concentration difference between the electrode surface and the electrode–electrolyte interface as follows [15, 20 and 21],

$$\eta_{con,a} = \frac{RT}{2F}\ln\left(P_{H_2}^0 / P_{H_2}^I\right),\ \ \eta_{con,c} = \frac{RT}{2F}\ln\left(\left(\frac{P_{O_2}^0}{P_{O_2}^I}\right)^{0.5} \times \frac{P_{H_2O}^I}{P_{H_2O}^0}\right) \tag{28}$$

The dusty gas model (DGM) is employed to describe both diffusion and permeation phenomena within the porous electrode [18 and 20],

$$\frac{J_{m,i}}{D_{i,k}^{eff}} + \sum_{j=1,\, j\neq i}^{n} \frac{y_j J_{m,i} - y_i J_{m,j}}{D_{ij}^{eff}} = -\frac{1}{RT}\left[P\frac{dy_i}{dx} + y_i\frac{dp}{dx}\left(1 + \frac{B_g P}{D_{i,k}^{eff} v_m}\right)\right] \tag{29}$$

where $D_{i,k}^{eff}$ is the effective Knudsen diffusion coefficient of species i; D_{ij}^{eff} represents the effective binary diffusion coefficient of species i and j [39, 40]; y_i represents the molar fraction of species i; and v_m is the dynamic viscosity of the gas mixture which is obtained by Wilke's method [40].

4. Results and Discussions

The values of thicknesses of the electrodes and electrolyte, along with cell properties used in the model are listed in Table 1. The pre-factors of exchange current densities, proton conductivities and electron hole conductivities are obtained by fitting the experimental data, as collected in Table 2. As mentioned in the previous section, the proposed models are applied to predict all the electrochemical-related variables (i.e., *J-V* curve, power output, possible potential losses and leakage currents) as well as fuel cell

efficiencies.

4.1. Model validation

The simulating *J-V* and power density performances of the H-SOFC are summarized in Fig. 3, compared with experimental data (symbols) with a temperature ranging from 550 ^{o}C to 700 ^{o}C. Overall, the mathematical model is able to reproduce the experiments relatively well except for some points at 700 ^{o}C. A possible reason for the failure is that the BZY electrolyte has high oxygen iron conduction at high operating temperatures, which is not considered in this model.

As shown in Fig. 3, the open-circuit voltage (OCV) values for all ranges of operating temperatures are lower than 1.0 V, suggesting that electronic leakages are considerable and can not be ignored. Specially, OCV values slightly drop with the increasing operating temperature, indicating that electronic leakages become more significant in higher temperature. In addition, the peak power densities together with the corresponding output voltages are collected in Table 3, which will be discussed together with Energy efficiencies.

4.2. Possible overpotential losses

Calculated anode and cathode activation polarizations for different operating temperatures are displayed in Fig. 4. The activation polarization increases steeply at low current densities and gradually at high current densities. The cathode polarization is obviously higher than that of the anode, because the electrochemical reduction of O_2 in the cathode is slower than the reduction of H_2 at the anode. Furthermore, the figure

clearly shows that both the anode and the cathode activation polarizations decrease with the increasing operating temperature. This is because the exchange current density increases as the temperature rises.

As shown in Fig. 5, the anode or cathode concentration overpotentials are all insignificant for all ranges of operating temperatures, due to that small cathode surfaces (0.33 cm^2) and large fuel flow rates (30 ml/min) were applied in the experiment. There is a strong linear relationship between cathode concentration polarizations and current density. Although the anode supported configuration is adopted in the button cell, the anode concentration overpotential is still dramatically lower than that at the cathode side. Generally there are two factors contributing to such small anode concentration polarization. One is that the transport resistance of hydrogen is lower than that of oxygen. The other is that no product species needs to leave the reaction site near the anode-electrolyte interface.

Under our operating conditions, the maximum loss is the electrolyte Ohmic polarization, as shown in Fig. 6. The Ohmic overpotential increases linearly with the current density for all the operating temperatures. One interesting finding is that the Ohmic overpotentials for higher temperature are larger when the current density is lower than 0.2 A/cm^2. Such results are obviously different from those obtained by the models without current leakage. This can be explained by that both proton conductivities and electron hole conductivities increase with growing operating temperatures. Therefore, the leakage currents at higher temperature are generally larger

than that at lower temperature. Based on Eq. (20) and Eq. (24), the Ohmic losses at higher temperature can be greater when the external current density is pretty low.

4.3. Leakage currents together with Faraday efficiencies

The leakage current densities as well as the Faraday efficiencies are determined as a function of cell voltages for all ranges of operating temperatures, as presented in Fig. 7. Overall, leakage currents increase with the increasing cell output voltage for all temperatures. The diving force of electron holes across the electrolyte increases resulting from external current densities decrease with the output voltages, as indicated by Eq. (21). Simultaneously, leakage current densities vary with cell operating temperatures, i.e., leakage current densities grow slowly at lower temperatures while increase rapidly at higher temperature. This is attributed to the heavy dependence of electron hole conductivity on temperatures.

The Faraday efficiency decreases with the increasing cell voltages for all ranges of temperatures, as shown in Fig. 7. The Faraday efficiencies at low temperature are generally higher than those at the high temperature. At higher cell voltages, especially above 0.7 V, the decreasing rate of Faraday efficiency is faster than that at lower voltages. All the above analysis indicates that current leakage can remarkably worsen the H-SOFC performance near open circuit condition.

4.4. Energy efficiency analysis for H-SOFCs

Energy efficiencies are expressed as a ratio of the generated electric power to the lower heating value of the fuel [41 and 42].

$$\eta_{en} = \frac{V_{out} \times J_{ext}}{N_{H_2} \times LHV_{H_2}} \tag{30}$$

The flow rate of the consumed H_2 can be determined by

$$N_{H_2} = \frac{J_{H^+}}{2F} \tag{31}$$

The model-predicted energy efficiencies versus cell voltages at different operating temperatures are presented in Fig. 8. Similar with Faraday efficiency, energy efficiencies at low temperature are also higher than those at high temperature. This is because the fact that leakage current would be increasingly visible at higher temperature. Overall, the highest energy efficiencies are observed when the output voltages range from 0.6 V to 0.8 V. Current leakage primarily influences the energy efficiencies near the open circuit condition. Another interesting finding is that the energy efficiencies for different temperatures gradually reach an identical level with decreasing output voltages.

The H-SOFC would be expected to work at the situation of peak power density. All the performances related to peak power density are collected in Table 3. The output voltages usually range from 0.4 V to 0.5 V, which are lower than the voltages for the highest energy efficiencies. In addition, the transfer numbers are listed and compared with Faraday efficiencies as well as energy efficiencies. Obviously, they are essentially different with each other due to transfer numbers would not change with external current. Moreover, the transfer numbers gradually decrease with the growing operating temperature, which is indicated that electron hole conductivities become increasingly

vital at higher temperatures.

5. Conclusions

In this work, the mechanisms of current leakage were discussed by assuming four electrode reactions (*RI-RIV*). In oxidizing atmospheres, protons react with oxygen to generate steam and electron holes at the cathode side. Current leakage occurs when electron holes pass through the electrolyte and combine with electrons at the anode side. Simultaneously, the Nernst-Planck equation was adopted to describe the relationship between protons and electron holes in the electrolyte. An analytical solution of leakage currents for H-SOFCs was deducted. Then, a mathematical model which considers porous media transport in the electrodes, electrochemical polarization at the interfaces, proton and electron hole conductions in the electrolyte was proposed. Using this model, all possible potential losses, leakage current density, Faraday and energy efficiencies were predicted.

Furthermore, Working H-SOFCs with BZY electrolyte, NiO-BZY anode and LSCF cathode accompanied with PNM nanoparticles were fabricated and tested. A good compatibility was observed between the experimental data and model-predicted results. The simulation results indicated that the maximum loss was still the electrolyte Ohmic overpotential, although the anode-support configuration was applied in the experiment. Another important finding is that current leakage primarily influences the H-SOFC performance when the output voltages are close to the OCV. This is because there is

usually the greatest gradient of electrochemical potentials in the electrolyte under OCV condition. Moreover, both Faraday efficiencies and energy efficiencies decrease with increasing operating temperatures under our operating condition. This is due to that the electron hole conductivity of BZY electrolyte grows faster than that of protons with increasing temperature. This study could provide some theoretical guidelines for the design and optimization of the H-SOFCs with current leakage.

Acknowledgements

This research was financially supported by the *Natural Science Foundation of China* (NSFC Grant No. 51778504; Grant No. 51304233; NSFC Grant No. 51208192), *Shenzhen Basic Research Project* (Grant No. JCYJ20160523160857948), *Joint Zhuzhou - Hunan Provincial Natural Science Foundation* (Grant No. 2018JJ4064), *National Defenses Research Funds for the Central Universities* (Grant No. 2042018gf0031), and *National Key Basic Research Program of China* (973 Program, Grant No. 2014CB239203).

We're grateful to the financial support from the US Department of Energy SECA Core Technology Program (under award number DE-FE0031176). Finally, the first author would like to gratefully acknowledge financial support from China Scholarship Council (No. 201706270100).

References

[1]. R. O'hayre, S. Cha, W. Colella, F. Prinz, Fuel cell fundamentals, John Wiley & Sons (2016).

[2]. B. C. Steele, A. Heinzel, *Nature* 414 (2001) 345-352.

[3]. R. M. Ormerod, Solid oxide fuel cells. *Chem. Soc. Rev.* 32, 17-28 (2003).

[4]. E. Fabbri, L. Bi, D. Pergolesi, E. Traversa, *Adv. Mater.* 24 (2012) 195-208.

[5]. K.-Y. Park, T.-H. Lee, S. Jo, J. Yang, S.-J. Song, H.-T. Lim, J. H. Kim, J.-Y. Park, *J. Power Sources* 336 (2016) 437-446.

[6]. F. Lefebvre-Joud, G. Gauthier, J. Mougin, *J. appl. Electrochem.* 39 (2009) 535-543.

[7]. E. Fabbri, D. Pergolesi, E. Traversa, *Chem. Soc. Rev.* 39 (2010) 4355-4369.

[8]. C. Duan, J. Tong, M. Shang, S. Nikodemski, M. Sanders, S. Ricote, A. Almansoori, R. O'Hayre, *Science* 349 (2015) 1321-1326.

[9]. D. Han, Y. Noda, T. Onishi, N. Hatada, M. Majima, T. Uda, *Int. J. Hydrogen Energy* 41 (2016) 14897-14908.

[10]. D. Pérez-Coll, G. Heras-Juaristi, D. P. Fagg, G. C. Mather, *J. Power Sources* 245 (2014) 445-455.

[11]. K. Nomura, H. Kageyama, *Solid State Ionics* 178 (2007) 661-665.

[12]. W. Wang, A. V. Virkar, *J. Power Sources* 142 (2005) 1-9.

[13]. A. Magrasó, *J. Power Sources* 240 (2013) 583-588.

[14]. M. Ni, *Int. J. Energy Res.* 34 (2010) 1027-1041.

[15]. Y. Patcharavorachot, N.P. Brandon, W. Paengjuntuek, S. Assabumrungrat, A. Arpornwichanop, *Solid State Ionics* 181 (2010) 1568-1576.

[16]. H. Liu, Z. Akhtar, P. Li, K. Wang, *Energies* 7 (2014) 173-190

[17]. M. Bavarian, M. Soroush, *J. Process Contr.* 22 (2012) 1521-1530

[18]. V. Menon, A. Banerjee, J. Dailly, O. Deutschmann, *Appl. Energ.* 149 (2015) 161-175.

[19]. M. Ni, Z. Shao, K.Y. Chan, *Energies* 7 (2014) 4381-4396.

[20]. M. Ni, D. Y. Leung, M. K. Leung, *J. Power Sources* 183 (2008) 133-142.

[21]. A. Arpornwichanop, Y. Patcharavorachot, *Chem. Eng. Res. Des.* 91 (2013) 1508-1516.

[22]. Y. Kalinci, I. Dincer, *Int. J. Hydrogen Energy* 43 (2018) 5795-5807.

[23]. M. Ni, D. Y. Leung, M. K. Leung, *J. Power Sources* 183 (2008) 682-686.

[24]. D.K. Lim, C.J. Park, M.B. Choi, C.N. Park, S.J. Song *Int. J. Hydrogen Energy* 35 (2010) 10624-10629.

[25]. D. Poetzsch, R. Merkle, J. Maier, *Adv. Funct. Mater.* 25 (2015) 1542-1557.

[26]. D. Poetzsch, R. Merkle, J. Maier, *Faraday Discuss.* 182 (2015) 129-143.

[27]. R.J. Kee, H. Zhu, B.W. Hildenbrand, E. Vøllestad, M.D. Sanders, R.P. O'Hayre, *J. Electrochem. Soc.* 160 (2013) F290-F300.

[28]. H. Zhu, S. Ricote, W.G. Coors, R.J. Kee, *Faraday Discuss.* 182 (2015) 49-74.

[29]. L. Lei, Z. Tao, T. Hong, X. Wang, F. Chen, *J. Power Sources* 389 (2018) 1-7.

[30]. D. Cui, Q. Liu, F. Chen, *J. Power Sources* 195 (2010) 4160-4167.

[31]. T. Nagasawa, K. Hanamura, *J. Power Sources* 290 (2015) 168-182.

[32]. F. He, T. Wu, R. Peng, C. Xia, *J. Power Sources* 194 (2009) 263-268.

[33]. S. Shen, L. Guo, H. Liu, *Int. J. Hydrogen Energy* 38 (2013) 1967-1975.

[34]. S. Shen, Y. Yang, L. Guo, H. Liu, *J. Power Sources* 256 (2014) 43-51.

[35]. R. Singh, K. T. Jacob, *Int. J. Eng. Sci*. 42 (2004) 1587-1602.

[36]. A. V. Virkar, *J. Power Sources* 194 (2009) 753-762.

[37]. N. Kurita, N. Fukatsu, K. Ito, T. Ohashi, *J. Electrochem. Soc.* 142 (1995) 1552-1559.

[38]. J.-H. Zhang, L.-B. Lei, D. Liu, F.-Y. Zhao, F. Chen, H.-Q. Wang, *Energ. Convers. Manage.* 14 (2017) 646-659.

[39]. H. Zhu, R. J. Kee, *J. Power Sources* 117 (2003) 61-74.

[40]. B. E. Poling, J. M. Prausnitz, O. C. John Paul, R. C. Reid, The properties of gases and liquids, Mcgraw-Hill New York, (2001).

[41]. F. Ishak, I. Dincer, C. Zamfirescu, *J. Power Sources* 212 (2012) 73-85.

[42]. F. Calise, M.D. Accadia, A. Palombo, L. Vanoli, *Energy* 31 (2006) 3278-3299

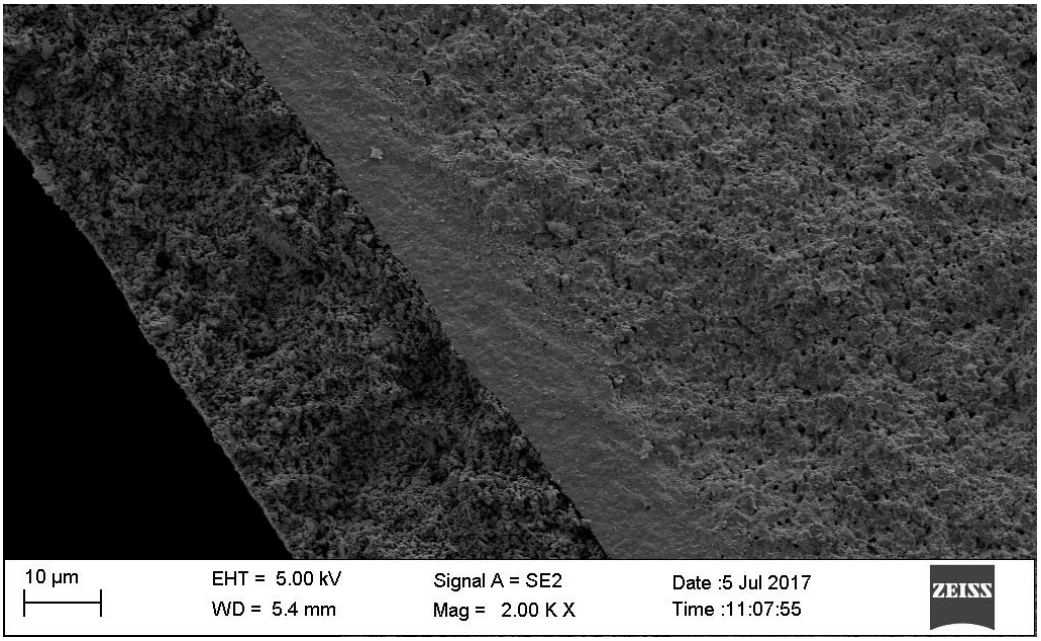

Fig. 1. Cross-sectional SEM graph of a single button fuel cell

Figure 2

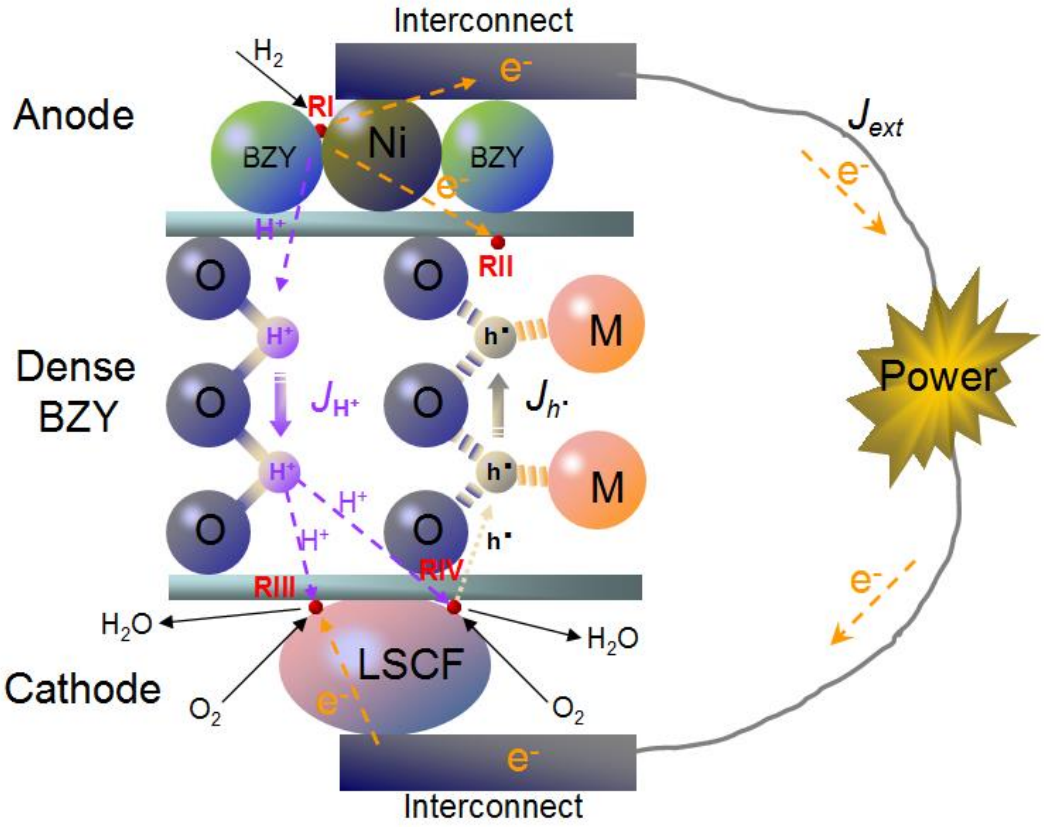

Fig. 2. The framework of charge transports in a solid oxide fuel cell based on proton-conducting electrolytes.

Figure 3

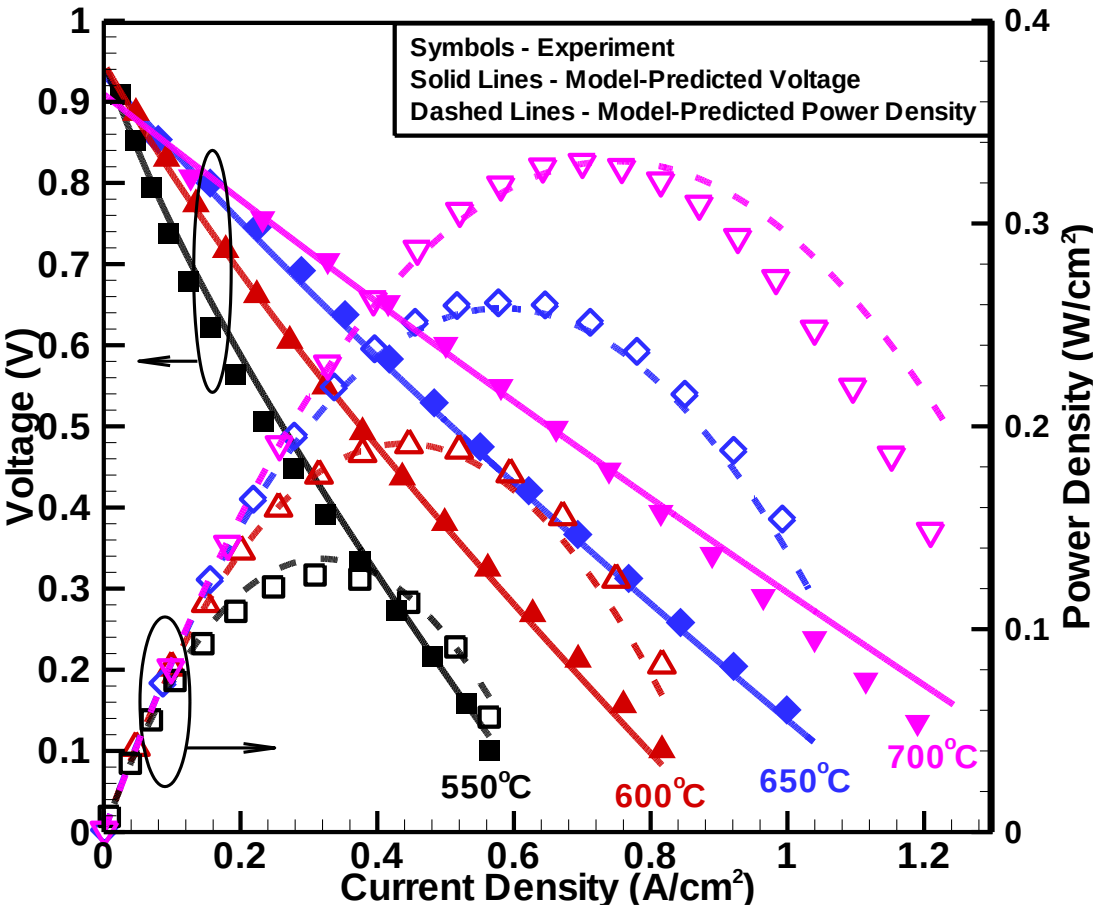

Fig. 3. Comparison of model-predicted and experimental J-V and power density curves for an H-SOFC operated at different temperatures.

Figure 4

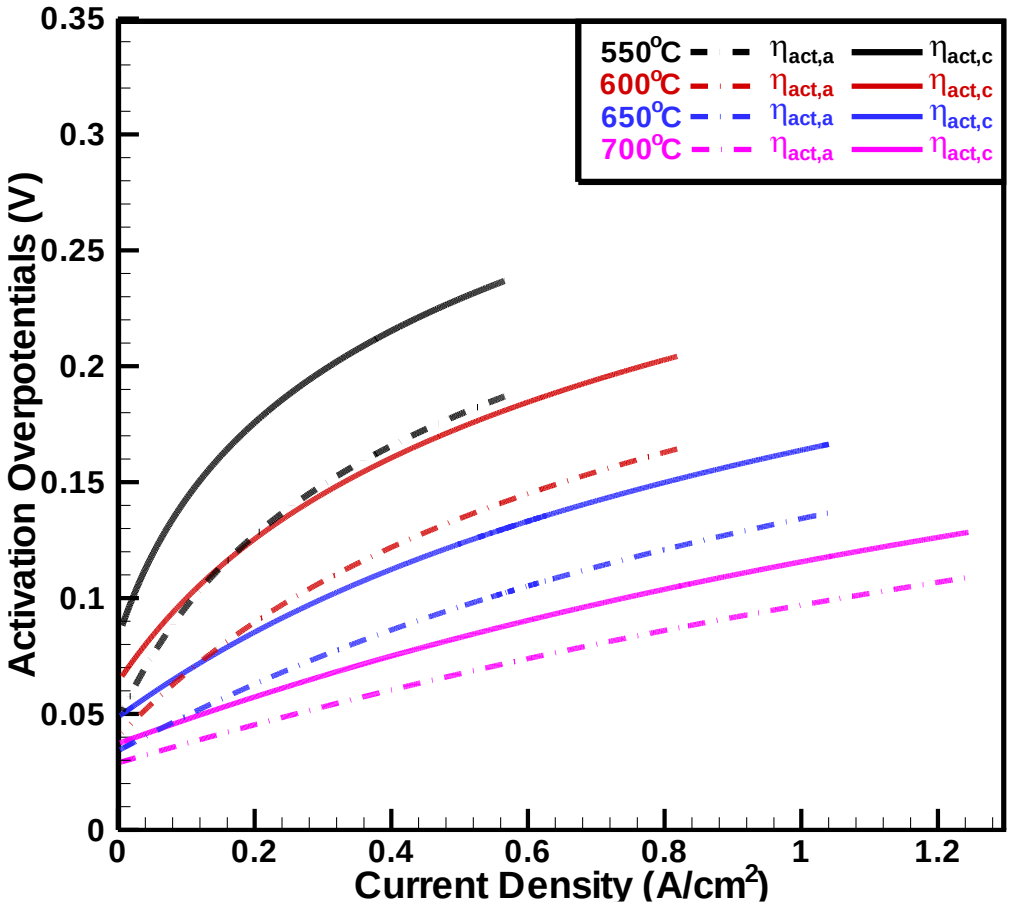

Fig. 4. Model-predicted activation overpotentials versus current density for an H-SOFC operated at different temperatures.

Figure 5

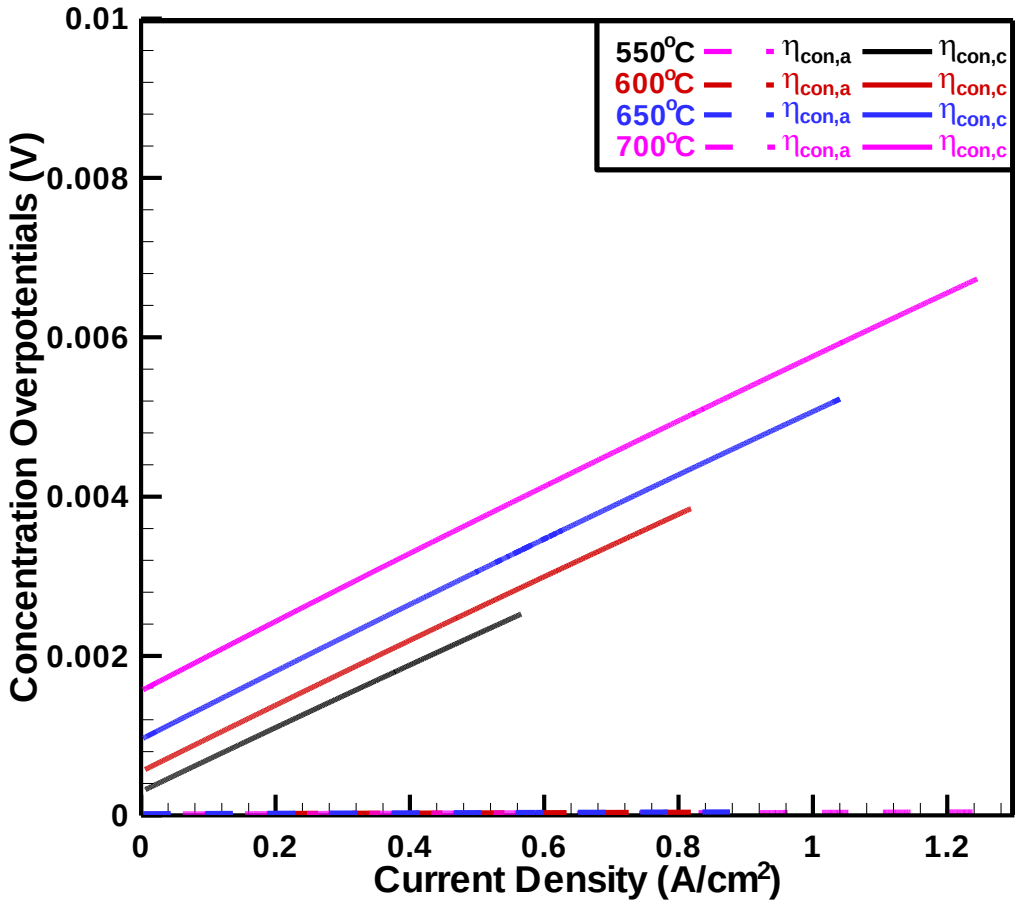

Fig. 5. Model-predicted concentration overpotentials versus current density for an H-SOFC operated at different temperatures.

Figure 6

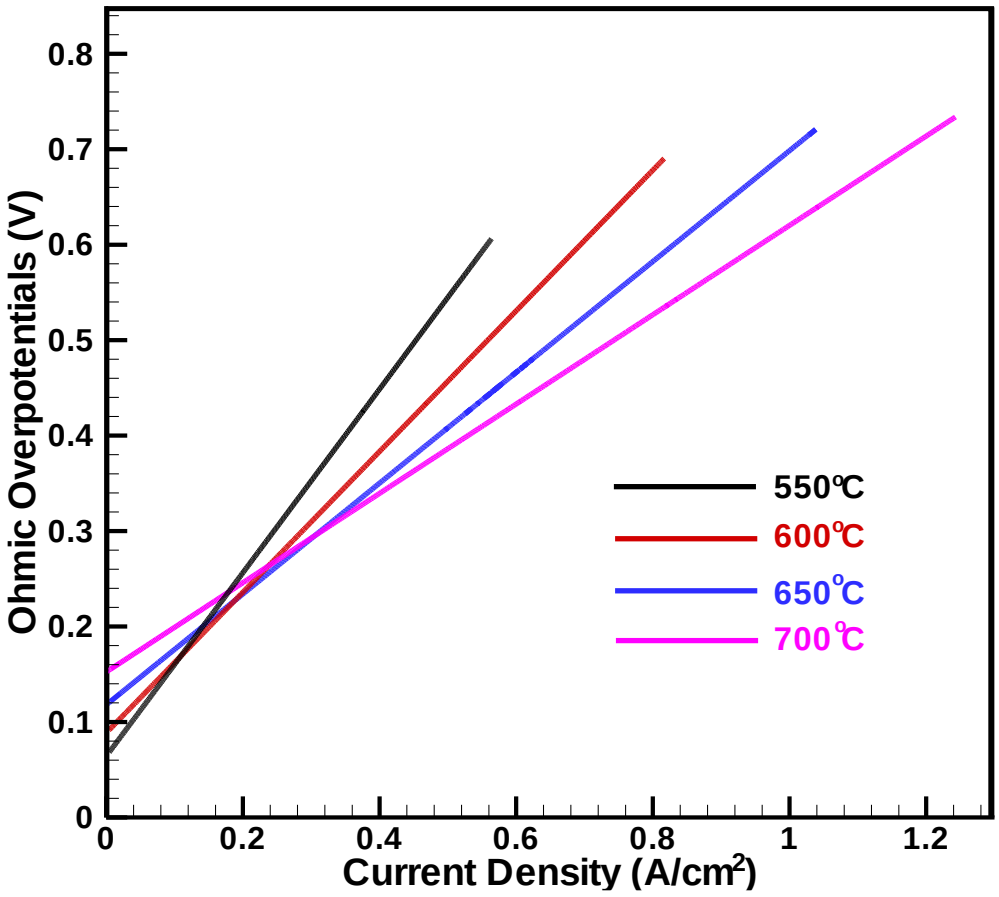

Fig. 6. Model-predicted Ohmic losses versus current density for an H-SOFC operated at different temperatures.

Figure 7

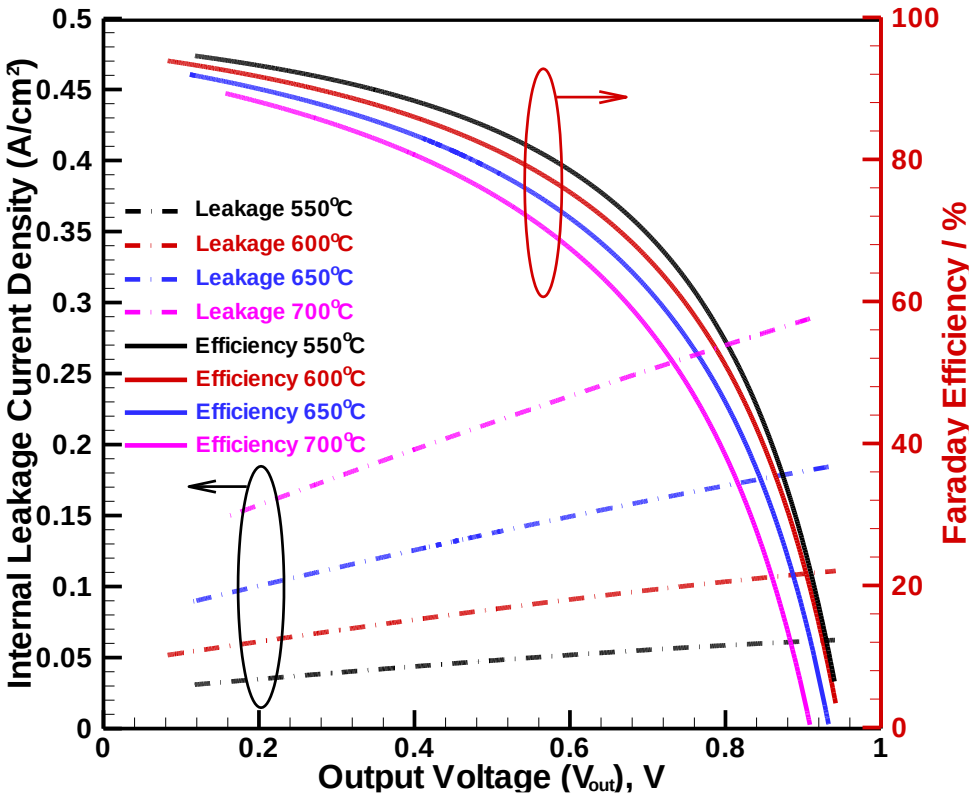

Fig. 7. Model-predicted electronic leakage current densities and Faraday efficiencies versus cell voltages at different operating temperatures.

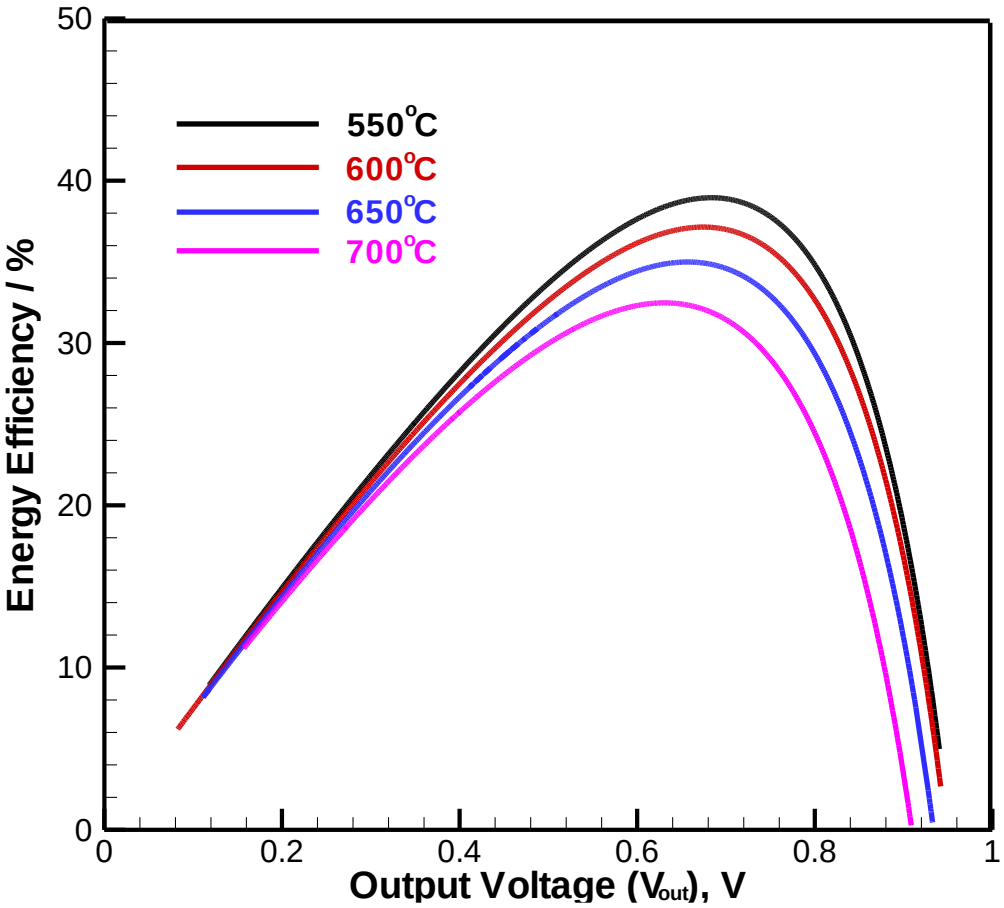

Fig. 8. Model-predicted energy efficiencies versus cell voltages at different operating temperatures.

Table 1 Cell parameters and properties used for modeling analyses [7, 38]

Parameter	Value
Operating temperature (T, ^{o}C)	550, 600, 650 ,700
Operating pressure (P, bar)	1.0
Anode inlet fuel molar ratio, (H_2/H_2O)	0.97/0.03
Anode	
Thickness (τ_a, μm)	550
Porosity (ε_a)	0.3
Tortuosity (ξ_a)	3.0
Average pore radius (r_p, μm)	0.5
Average particle diameter (d_p, μm)	10
activation energy ($E_{act,a}$, J/mol) [18, 20]	100000
Cathode	
Thickness (τ_c, μm)	40
Porosity (ε_c)	0.3
Tortuosity (ξ_c)	3.0
Average pore radius (r_p, μm)	0.5
Average particle diameter (d_p, μm)	10
activation energy ($E_{act,a}$, J/mol) [18, 20]	120000
Electrolyte	
Thickness (τ_{ele}, μm)	15
Activation energy for proton carrier (E_{H^+}, eV) [11]	0.38
Activation energy for electronic hole carrier ($E_{h^{\cdot}}$, eV) [11]	0.73

Table 2 Electrochemical model/input parameters fitted with experimental data.

Exchange current density parameters	
pre-exponential factor of exchange current (γ_a, A/m^2)	9.577×10^8
pre-exponential factor of exchange current (γ_a, A/m^2)	8.817×10^9
Electrolyte conductivity parameters	
Pre-factor of proton conductivity($\sigma_{0,H+}$, S·m^{-1}°C)	25719.4
pre-factor of electron hole conductivity ($\sigma_{0,h^{\cdot}}$, S·m^{-1}°C)	212139.6

Table 3 Cell performances at peak power density for different operating temperatures.

Operating temperature (T), ^{o}C	550	600	650	700
Peak power density, W/cm^2	0.127	0.191	0.262	0.330
Output voltage (V_{out}), V	0.41	0.44	0.46	0.45
Faraday efficiency (%)	88.1	84.5	80.7	78.1
Energy efficiency (%)	29.1	29.7	29.8	28.1
Transfer number	0.918	0.895	0.868	0.840